Physics of Plasmas

Nonlinear interactions of ion acoustic waves explored using fast imaging decompositions

Cite as: Phys. Plasmas **30**, 012109 (2023); https://doi.org/10.1063/5.0131745
Submitted: 24 October 2022 • Accepted: 19 December 2022 • Published Online: 20 January 2023

Simon Vincent, Vincent Dolique and Nicolas Plihon

COLLECTIONS

This paper was selected as Featured

View Online Export Citation CrossMark

ARTICLES YOU MAY BE INTERESTED IN

Banded chorus generation by an electron shell distribution in an inhomogeneous magnetic field: 1D PIC simulations
Physics of Plasmas **30**, 012904 (2023); https://doi.org/10.1063/5.0127471

Sheath near a negatively biased electron-emitting wall in an ion-beam-plasma system and its implication to experimental measurement
Physics of Plasmas **30**, 013510 (2023); https://doi.org/10.1063/5.0126650

Guided electromagnetic discharge pulses driven by short intense laser pulses: Characterization and modeling
Physics of Plasmas **30**, 013105 (2023); https://doi.org/10.1063/5.0124011

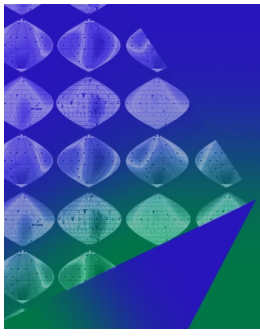

Physics of Plasmas
Features in Plasma Physics Webinars
Submit Today!

AIP Publishing

© 2023 Author(s).

Physics of Plasmas ARTICLE scitation.org/journal/php

Nonlinear interactions of ion acoustic waves explored using fast imaging decompositions

Cite as: Phys. Plasmas **30**, 012109 (2023); doi: 10.1063/5.0131745
Submitted: 24 October 2022 · Accepted: 19 December 2022 ·
Published Online: 20 January 2023

View Online Export Citation CrossMark

Simon Vincent,[1,2,a)] Vincent Dolique,[1] and Nicolas Plihon[1]

AFFILIATIONS

[1]Univ Lyon, ENS de Lyon, CNRS, Laboratoire de Physique, F-69342 Lyon, France
[2]École Polytechnique Fédérale de Lausanne (EPFL), Swiss Plasma Center (SPC), CH-1015 Lausanne, Switzerland

[a)]Author to whom correspondence should be addressed: sph.vincent@protonmail.com

ABSTRACT

Fast camera imaging is used to study ion acoustic waves propagating azimuthally in a magnetized plasma column. The high-speed image sequences are analyzed using proper orthogonal decomposition and 2D Fourier transform, allowing to evaluate the assets and differences of both decomposition techniques. The spatiotemporal features of the waves are extracted from the high-speed images, which highlight energy exchanges between modes. Growth rates of the modes are extracted from the reconstructed temporal evolution of the modes, revealing the influence of ion-neutral collisions as pressure increases. Finally, the nonlinear interactions between modes are extracted using bicoherence computations, and they show the importance of interactions between modes with azimuthal wave numbers m, $m-1$, and -1, with m as an integer.

© 2023 Author(s). All article content, except where otherwise noted, is licensed under a Creative Commons Attribution (CC BY) license (http://creativecommons.org/licenses/by/4.0/). https://doi.org/10.1063/5.0131745

I. INTRODUCTION

The propagation of ion sound waves or ion acoustic waves is ubiquitous in plasmas, and their nonlinear interactions, possibly leading to ion acoustic turbulence, are a widespread energizing process in plasma physics. The nonlinear evolution of ion acoustic waves (IAW) generically leads to instabilities and the development of nonlinear structures. For instance, IAW have long been observed in the solar wind and have been related to the anisotropy of the electron distribution function distribution function.[1] In this context, IAW are driven unstable when the ratio of the electron to ion temperature is larger than unity, as observed by the Helios spacecraft,[2] and very recently for oblique IAW by the Parker Solar Probe.[3] Heating of energetic particles from ion acoustic turbulence was also proposed in the context of polar aurorae.[4] The nonlinear evolution of ion acoustic waves into strongly nonlinear structures, such as solitons[5] or double layers, has been reported in electropositive plasmas[6] or electronegative plasmas[7] for which two branches of ion acoustic waves exist.[8] In the context of bounded plasmas, IAW excited in sheaths may affect particle transport at low pressure[9] or lead to strong ion heating[10] when the ratio of the electron to ion temperature is larger than unity. IAW may also be useful tools to probe sheath criteria in multiple ion plasmas.[11–13] Technological plasmas may also trigger IAW that, in return, affect their operation, as reported for Hollow Cathodes,[14,15] Hall thrusters,[16] and diverging magnetic nozzle thrusters.[17]

In this article, we report on the observation of localized ion acoustic waves in a magnetized plasma column using high-speed camera imaging. Thus, our observations shed new light on the ion acoustic activity that has been previously reported in similar configurations.[18–24] We do not investigate the origin of the IAW from parametric instability or wave interactions here, as was done in these previous investigations, but we analyze the spatiotemporal characteristics of the IAW using mode decomposition from high-speed imaging. The IAW nonlinear interactions are quantitatively highlighted by means of bicoherence computations.

The article is organized as follows. The experimental setup is introduced in Sec. II. The analysis of fast camera measurements by mode decomposition techniques is presented in Sec. III. In particular, we highlight the differences and complementarities of two different mode decompositions, namely proper orthogonal decomposition and 2D Fourier transform. In Sec. IV, the waves observed by camera imaging are identified to be IAW from the wave phase velocities. Finally, the nonlinear mode interactions are characterized, and their nonlinear aspect is exhibited in Sec. V, and conclusions are drawn in Sec. VI.

II. EXPERIMENTAL SETUP AND DIAGNOSTICS

A. Experimental setup

The experimental setup[25] consists of a 20 cm diameter, 1 m long stainless steel cylindrical chamber containing an argon plasma

© Author(s) 2023

generated by a 1 kW, 13.56 MHz radio frequency source. The coordinates will be referenced using a cartesian coordinate system, where z denotes the axial direction (see Fig. 1). A cylindrical coordinate system (r, θ, z) will be used for the reconstruction of rotating modes. The plasma base pressure p_0 in the chamber is regulated at a fixed value, between 0.8 and 2 mTorr by steps of 0.1 mTorr. The plasma is created by an inductive source around a 11 cm diameter borosilicate tube connected at one end of the chamber (at $z = 0$ cm). Three coils placed along the steel cylinder generate an axial magnetic field that confines the plasma (see Fig. 1). This magnetic field is not perfectly homogeneous along z. For a current in the coils set here at 100 A, it has an averaged amplitude along the z-axis of $B = 170$ G.

Radial profiles of the plasma density n, the electron temperature T_e, and the plasma potential Φ_p are performed using a five-tip probe[26,27] and an emissive probe, respectively. The probes were inserted radially at $z = 49$ cm (see blue dashed line in Fig. 1). To keep the whole apparatus in a steady thermal state, the operation of the plasma is pulsed: the plasma is sustained over typically 5 s, during which data are acquired, with a repetition period of typically 30 s. The experiment is fully automated to allow high repeatability and reproducibility of the plasma. The level of shot to shot reproducibility was $\pm 0.6\%$ for the ion saturation current of a Langmuir probe, with a standard deviation of 0.2% (estimated from a series of 40 shots at the plasma column center). Radial scans of the plasma parameters were performed sequentially: each spatial point has been acquired during one plasma-pulse, and the probe is translated between two pulses, from the center of the plasma column ($r = 0$ cm) to its edge ($r = 10$ cm).

The results presented in this article mainly rely on high-speed imaging of the plasma emitted light, performed through a DN 200 borosilicate window closing the chamber at $z = 80$ cm (opposite to the source tube). A Phantom v2511 camera is placed along the z-axis, 3.5 m away from this window, and the light intensity naturally radiated by the plasma I_{cam} is captured at 200 kfps with a resolution of 256×256 px. A filter around 750 ± 5 nm is used in order to restrict the collected light to a single ArI spectral line. Examples of the mean intensity $\langle I_{\text{cam}} \rangle$ and fluctuation standard deviation $\sigma(\tilde{I}_{\text{cam}})$ images are shown in Fig. 1. Note that the plasma column is not perfectly axisymmetric, and the fluctuations are of the order of 10% of the mean amplitude. Note also that the depth of field of the optical setup being of the order of the length of the chamber (with a camera objective aperture set at f/4, and a focal length of 135 mm), the light intensity recorded by the camera is actually the result of an integration along the z-axis. Due to the magnetic field ripple and the parallax, a direct comparison of the probes' measurements (at $z = 49$ cm) and the camera images (where light is integrated along z) is not relevant. Thus, we introduce a distorted space (x^*, y^*, and z) in which the camera lines of sight are parallel (see Ref. 27 for more details). The camera images are, hence, observed in the plane (x^*, y^*), which may also be referenced as (r^*, θ) in a polar coordinate system.

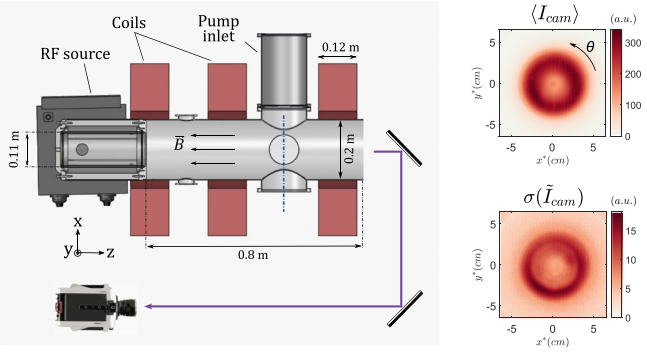

FIG. 1. Left: sketch of the experimental setup. The dashed blue line indicates where probe profiles are measured. Right: mean image of the light intensity collected by the camera (top), and standard deviation of the fluctuations around this average value (bottom), for $p_0 = 1$ mTorr.

B. Radial profiles of the plasma parameters

The top row of Fig. 2 displays the radial profiles of the plasma density, electron temperature, and plasma potential as a function of r for a pressure $p_0 = 1$ mTorr. As previously introduced, these profiles cannot be directly compared to the images in the (r^*, θ) plane. However, assuming axisymmetry and invariance of the plasma parameter along magnetic field lines, a synthetic integration process detailed in Ref. 27 allows to map the probe measurements along r (at $z = 49$ cm) to the images expressed along r^*, enabling quantitative comparison. The density is approximately constant in the core region of the plasma for $r \leq 4$ cm ($r^* \leq 3$ cm) and then decreases toward the edge. A clear peak can be seen around $r = 4.5$ cm ($r^* \sim 3$ cm) for the electron temperature, produced by the higher ionization rate of the RF inductive source close to the wall at $r = 5.5$, $z \sim -10$ cm. This higher temperature is also responsible for the higher light emission observed on the images at $r^* \sim 3$ cm in Fig. 1. Finally, the plasma potential decreases from the center to $r \sim 4$ cm (i.e., $r^* \sim 3$ cm) and presents a strong positive gradient at the edge of the plasma column. This is responsible for an $\vec{E} \times \vec{B}$ drift that drives plasma rotation in the $-\vec{e}_\theta$ direction, discussed later in this work.

The radial profiles of the fluctuations of the plasma parameters are shown in the middle panel of Fig. 2. The fluctuations are peaked at the edge of the plasma column at $r \sim 5.5$ cm (i.e., $r^* \sim 4$ cm).

Filtered light fluctuations recorded by fast camera are usually considered to be a proxy for density fluctuations.[28–30] For the magnetic field value of $B = 170$ G reported in this article, simultaneous probe and camera measurements indeed showed the fluctuations of density $\tilde{n}$ and light intensity $\tilde{I}_{\text{cam}}$ at the probe location to have very similar spectra, as shown in the bottom panel of Fig. 2. However, as it was shown in our previous work,[27] for magnetic field values in the range 100 to 700 G, light intensity naturally radiated by low temperature plasmas are also highly correlated to the electron temperature. In Sec. IV, the comparison of experimental phase velocities with the theoretical ion acoustic speed nonetheless requires to assume $\tilde{I}_{\text{cam}}$ to be a reasonable proxy for $\tilde{n}$. We therefore underline that this is a rather strong assumption, and that for further quantitative comparison $\tilde{I}_{\text{cam}}$ should be interpreted as a combination of both $\tilde{n}$ and $\tilde{I}_e$ – a task beyond the scope of this article. The strong spectral component observed at 5.6 kHz is identified as a Kelvin–Helmholtz mode.[31] In the present work, we will focus on fluctuations observed between 50 and 70 kHz, which are unambiguously identified as ion acoustic waves.

III. IMAGE ANALYSIS

The first and most natural tool that comes to mind for the images analysis is the Fourier decomposition. This is used later on; we prefer

© Author(s) 2023

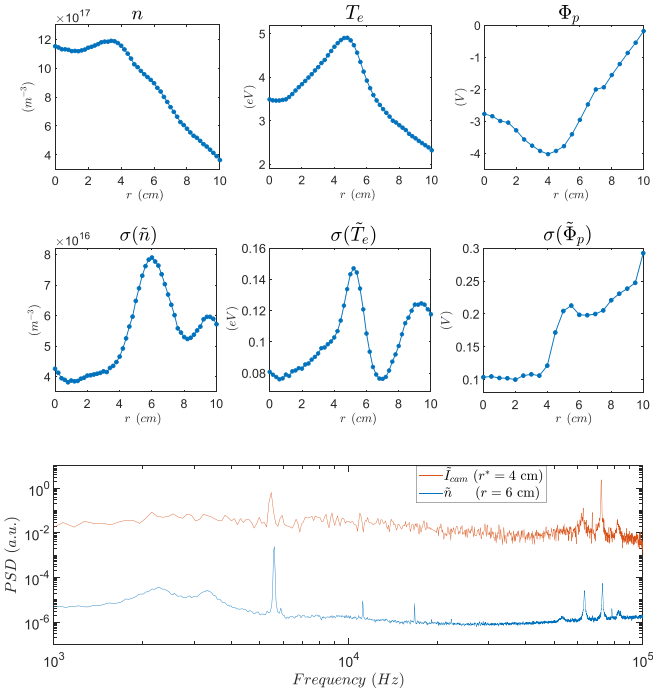

FIG. 2. Radial profiles of the density, electron temperature, and plasma potential mean values (top row) and fluctuations (middle row) at $p_0 = 1$ mTorr. Plasma parameter measurements were made with five tips (n, T_e) and emissive (Φ_p) probes. Bottom: power spectral density of the plasma density and light intensity fluctuations (computed from the average value of a 5×5 pixel box on the images).

here to start the analysis by using an alternative method, the proper orthogonal decomposition (POD).

Note that before performing these decomposition, we choose to normalize each pixel by its fluctuation mean, as was done in similar conditions.[32] This choice greatly enhances the contrast, allowing to nicely extract the relative amplitudes of the modes (especially in the regions of low light intensity), but at the cost of losing information on the absolute amplitude of the modes.

Note, finally, that in the following, the light fluctuations recorded by the camera $\tilde{I}_{\mathrm{cam}}$ will simply be denoted as I for easier readability.

A. Proper orthogonal decomposition

The POD consists in extracting the spatial structures that are dominant throughout time in a given dataset $I(\mathbf{r}^*, t)$, where $\mathbf{r}^*$ denotes space. This is done by computing the eigenmodes Ψ_i of the spatial autocorrelation of the time-averaged field $\langle I \rangle(\mathbf{r}^*)$. These so-called spatial modes Ψ_i then define an orthonormal basis onto which the original data can be projected. This can be written as

$$I(\mathbf{r}^*, t) = \sum_i \sigma_i\, a_i(t) \psi_i(\mathbf{r}^*),$$

with $\sigma_i\, a_i(t)$ being the time evolution of the data projected on the spatial modes Ψ_i. Here, a_i and Ψ_i are of norm unity; the amplitudes of the various components of the decomposition are, thus, given by the values of σ_i.

One of the most interesting aspects of this decomposition is that it is done without any *a priori* on the shape of the Ψ_i structures; they simply come out from the computation process, as *natural* modes, contrary to the Fourier analysis, which projects the data onto predefined spatial and temporal structures. Hence, POD might allow the emergence of structures with physical significance that are not well described by mere Fourier modes. Thanks, moreover, to its simplicity of implementation and computational speed when performed onto a discrete set of data, as is explained later, POD becomes a very attractive and efficient analysis tool for experimentalists, and it has grown very popular in the last few decades for the analysis of data from experiments or from numerical simulations. Note that depending on the field, this technique is also referred to as Karhunen–Loève decomposition (as a reference to the original mathematical theorem) or principal component analysis.

The set of spatial modes (Ψ_i) has the property of being the optimal basis for approximating the data I:[33] for any N, the norm of the projection of I onto $(\Psi_i)_{1,N}$, which reads $\sum_1^N \sigma_i^2$, is higher than the projection onto any other basis than one might choose. For a given value of N, the spatial modes $(\Psi_i)_{1,N}$ can then be interpreted as the vectors that are the best suited to reproduce the information carried by I, in the most efficient way. Applied to physical data, this property is even more interesting if the σ_i^2 values have a clear physical meaning. The use of POD on experimental data has been initiated in fluid dynamics for the analysis of turbulent velocity fields.[34] In this context, the norm $\sum_1^N \sigma_i^2$ of the projected data represents a kinetic energy, and the modes Ψ_i may then be interpreted as the most important flow structures in terms of kinetic energy. POD has then been applied to spatiotemporal measurements of plasma fluctuations in tokamaks, either measured by sets of Langmuir probes[35–37] or by means of soft x-ray emission.[38] It has also been applied to camera imaging data of naturally radiated plasma light to exhibit spiral shaped structure generated by a $m = 2$ instability in a linear device[39] and in a tokamak to highlight plasma response to resonant magnetic perturbations.[40] More recently, the technique was used to characterize instabilities in the plume of a Hall thruster from fast imaging data.[41] Following this study, POD has been applied to decompose the camera imaging data of a plasma plume produced by a high-current hollow cathode.[42] Unfortunately, in the latter cases, the physical interpretation of the Ψ_i vectors is not as straightforward as in fluid mechanics, since the extracted modes result from the decomposition of light intensity fields, which depends in a non-trivial way on the plasma parameters. Even by considering as a crude approximation $\tilde{I}_{\mathrm{cam}} \propto \tilde{n}$, not much can be said on the norm $\sum_1^N \sigma_i^2$ in terms of physical significance. This does not mean the amplitude of the modes extracted from plasma emitted light is void of meaning, but simply that one has to be careful before thinking of it as a precise energy estimation. In this article, POD decomposition is thus discussed in a purely qualitative way. Finally, POD does not require any symmetry, which is a significant advantage over Fourier decomposition for instance. In the case of complex geometries, POD can be an efficient alternative for capturing the physical structures in the data.

In practice, it can be shown that a direct extraction of the spatial modes Ψ_i associated with their temporal evolution a_i is, in fact,

© Author(s) 2023

achieved by applying a mere singular value decomposition (SVD) to the matrix containing the data I rearranged in such a way that one dimension of the matrix represents space, and the other time. This way of computing a POD, also referred to as bi-orthogonal decomposition,[43] is the one implemented here. Each image (of p pixels) of a video containing q frames is rearranged to form a matrix I of size p × q to which a singular value decomposition is applied, $I = \Psi\Sigma A^t$. Ψ and A are orthonormal matrices of respective sizes $p \times p$ and $q \times q$, and Σ is a matrix of the same size as I. The matrix Σ only contains diagonal elements, which are the decomposition's singular values σ_i,

$$\overbrace{\quad\quad}^{time}\left\{\begin{matrix}\\ space\\ \\ \\ \\ \end{matrix}\right.\begin{bmatrix} & & \\ & (I)_{ij} & \\ & & \end{bmatrix} = \begin{bmatrix} \vdots & \vdots \\ \Psi_1 & \Psi_2 \\ \vdots & \vdots \end{bmatrix} \begin{bmatrix} \vdots \\ \Psi_q \\ \vdots \end{bmatrix} \begin{bmatrix} \sigma_1 & & \\ & \ddots & \\ & & \sigma_q \end{bmatrix} \begin{bmatrix} \cdots a_1 \cdots \\ \cdots a_2 \cdots \\ \\ \cdots a_p \cdots \end{bmatrix}.$$

Figure 3(a) shows the result of a POD applied to a 100 ms time series of intensity fluctuations (i.e., 20 000 images) recorded at a pressure $p_0 = 1.3$ mTorr. The spatial modes $\Psi_i(\mathbf{r}^*)$ are displayed in the top row, the time series of the amplitudes $a_i(t)$ in the middle row, and the corresponding power spectral density $S(f)$ in the bottom row. The interpretation of the decomposition requires to consider pairs of modes, such as $I^{POD}_{1,2}(\mathbf{r}^*, t) = \sigma_1 a_1(t)\Psi_1(\mathbf{r}^*) + \sigma_2 a_2(t)\Psi_2(\mathbf{r}^*)$, which yields rotating azimuthal waves of the type $e^{-i\omega t - im\theta}$ (shown later in Subsection III C), since the spatial modes Ψ_1 and Ψ_2 are shifted by a quarter wavelength, and the temporal modes a_1 and a_2 are in quadrature [see Fig. 3(c)].[44] In the example shown in Fig. 3, the modes (Ψ_1, a_1) and (Ψ_2, a_2) correspond to a $m = -5$ rotating azimuthal wave, the modes (Ψ_3, a_3) and (Ψ_4, a_4) correspond to a $m = -6$ rotating azimuthal wave, and the modes (Ψ_6, a_6) and (Ψ_7, a_7) correspond to a $m = -4$ rotating azimuthal wave.

The rotation frequencies of the m-modes can be deduced from the spectra of the temporal signals a_i, shown in the bottom row of Fig. 3(a). A very clear peak at frequency $f = 55.6$ kHz is observed for the modes 1 and 2, capturing the $m = -5$ azimuthal wave. The $m = -6$ wave (POD modes 3 and 4) has a $f = 65.1$ kHz frequency, and the $m = -4$ wave (POD modes 6 and 7) has a $f = 45.2$ kHz frequency. Section IV shows that these modes are ion acoustic waves.

The singular values σ_i of the modes are plotted in Fig. 3(b). The amplitudes of σ_1 and σ_2 are nearly identical (within 0.3%), and more than twice larger than the other singular values, showing that the dynamics is dominated by a $m = -5$ rotating mode. The time series $a_i(t)$ show sudden changes in amplitude, for instance at times $t \sim 3.8$, 29.5, and 65.2 ms, corresponding to an energy exchange between modes $m = -6$ and -5, that will be investigated in Sec. V. The relatively intense POD mode (Ψ_5, a_5), with a strong spectral component

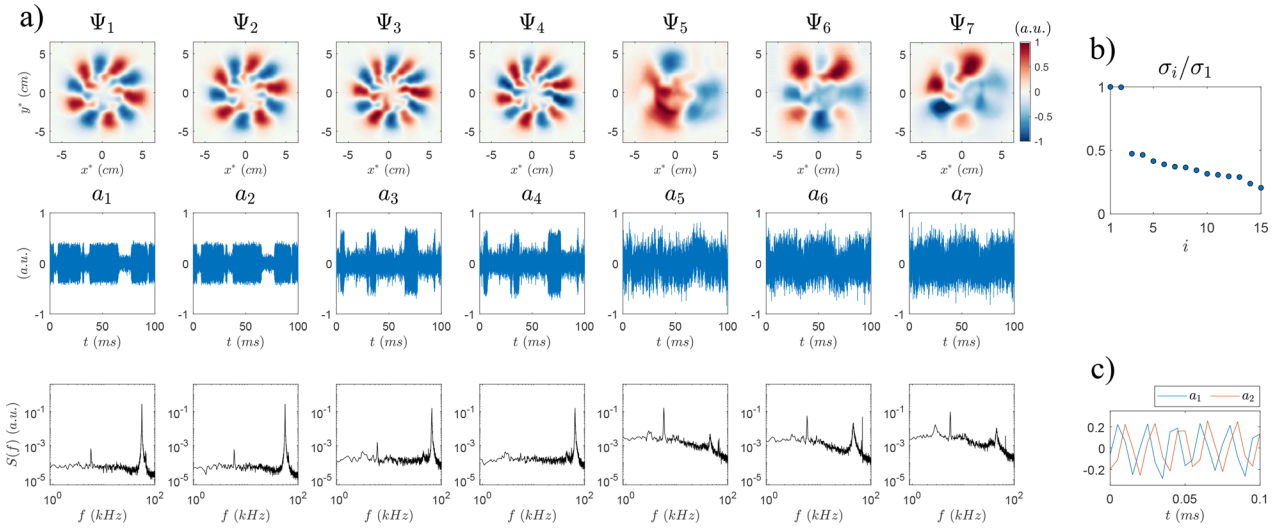

FIG. 3. Proper orthogonal decomposition modes (a) and singular values (b) of light intensity normalized fluctuations for $p_0 = 1.3$ mTorr. (c) Zoom on the evolution of a_1 and a_2. See text for details.

© Author(s) 2023

at $f = 5.6$ kHz, was identified as a $m = 3$ Kelvin–Helmoltz mode,[31] not discussed here. The POD analysis presented here was straightforward to implement, and it provides a very efficient way of extracting global features captured in a video sample. Now, we present the results of a Fourier analysis performed on the same data that complements the POD analysis.

B. 2D Fourier transform

The 2D Fourier Transform (2D-FT) of a two variables function $f(\mathbf{x}, t)$ reads $\hat{f}(\mathbf{k}, \omega) = \int\int f(\mathbf{x}, t) e^{-i(\mathbf{k}\cdot\mathbf{x}+\omega t)} d\mathbf{x}dt$. 2D-FT is classically used to decompose the spatiotemporal signals collected by azimuthally distributed probe arrays into azimuthal modes.[45,46] Following many studies using camera imaging and performed in the context of linear plasma devices[29,47–49] and plasma thrusters,[50,51] the 2D-FT is here performed on virtual rings at various radii r^*. For a given value of the radius r^*, a time series $I(\theta, t)|_{r^*}$ is extracted from the camera images. For each angle $\theta_n = \frac{2\pi n}{N_\theta}$ with $n \in [0 : N_\theta - 1]$, the value of the pixel at position (r^*, θ_n) is extracted. The angle resolution of $N_\theta = 700$ is chosen here, such that no interpolation is needed in the processes of converting either a ring of pixels in the image space (x^*, y^*) into a vector along the θ direction, nor in the inverse process, when reconstructing images in the (x^*, y^*) plane from the mode decomposition results. Since the images are 2π periodic in the θ direction, the wave vectors read m/r^*, with m as an integer, and the 2D-FT of $I(\theta, t)|_{r^*}$ is computed as

$$\hat{I_{r^*}}(m, f) = \int\int I(\theta, t)|_{r^*} e^{-i(m\theta + 2\pi f t)} d\theta dt,$$

with f as the frequency. The resulting 2D power spectrum $S_{r^*}(m, f) = |\hat{I_{r^*}}(m, f)|^2$ displays the amplitudes of light intensity fluctuations as a function of the spatial mode m and the frequency f, at a given radius r^*. Note that at radius $r^* \sim 3.5$ cm on the images, the intensity $I(\theta, t)|_{r^*}$ is reconstructed from a corona of ~400 pixels, which ensures a very good precision in the extraction of the first modes m up to $m \sim 20$. The power spectrum at $r^* = 3.3$ cm and $p_0 = 1.3$ mTorr is shown in Fig. 4. The observations are similar to those drawn from the POD analysis: the dominant mode is an $m = -5$ mode whose frequency is peaked at 55.6 kHz, and the other important modes are an $m = -6$ mode peaked at 65.2 kHz and an $m = -4$ mode peaked at 44.9 kHz. Note that this 2D power spectrum provides a dependence of the dominant frequency on the mode number; therefore, it can be seen as an experimental dispersion relation. This is used in Sec. IV for the identification of the modes.

The full spatiotemporal evolution of any given m-mode can also be extracted by 2D-FT. To this end, the 2D Fourier transform is computed for radii r^* covering the full image (here, 2D-FT is computed for $r^* = 2i$ px, $i \in [1 : 64]$, instead of $r^* = [1 : 128]$ px, to limit memory storage and increase computational speed). For the given m and r^* values, the inverse Fourier transform of $\hat{I}_{r^*}(m, f)$ is computed, resulting in the spatiotemporal signal of the m-mode, at radius r^*. Performing this inverse computation for all radii previously mentioned leads to the full spatiotemporal reconstruction of the m-mode. Examples of snapshots of such reconstructed 2D-FT modes are shown and commented in Subsection III C.

The average amplitude of the reconstructed modes is then computed along time, providing a global picture of the mode dynamics.

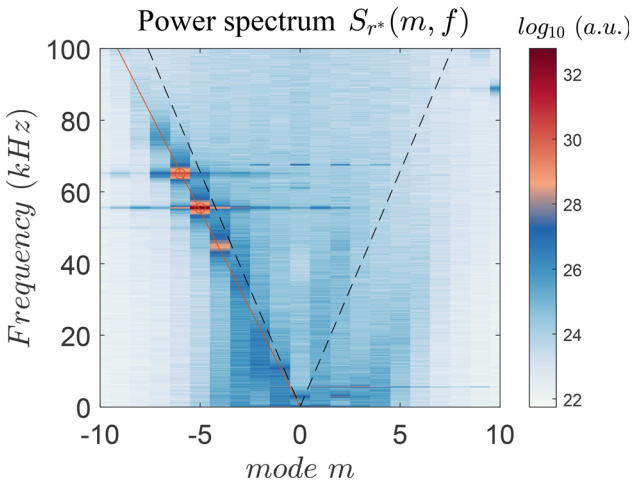

FIG. 4. Power spectrum of the raw light intensity fluctuations from camera imaging, taken on a corona of radius $r^* = 3.3$ cm for $p_0 = 1.3$ mTorr. Dispersion relations are plotted from experimental fits of the power spectrum maxima (red) and from the ion acoustic speed (black) (see Sec. IV).

The global m-mode time evolution for $p_0 = 1, 3$ mTorr is plotted in Fig. 5 (top). As already observed on the time signals of the POD in Fig. 3, clear exchange events can be observed involving modes $m = -5$ and -6. The $m = -4$ mode is seen to follow the dynamics of the $m = -5$ mode, while the $m = -7$ mode follows the dynamics of the $m = -6$ mode, a feature that was not detected by the POD analysis. From the reconstructed signals of the individual m-modes, the instantaneous mean radial profile is computed by an integration over θ, allowing for the computation of the radial location $r^*_{\max}$ where the wave amplitude is maximal. Figure 5 (bottom) shows $r^*_{\max}$ for the $m = -5$ and -6 modes, which are highly correlated with the global dynamics of the modes. Again this could not be deduced from POD,

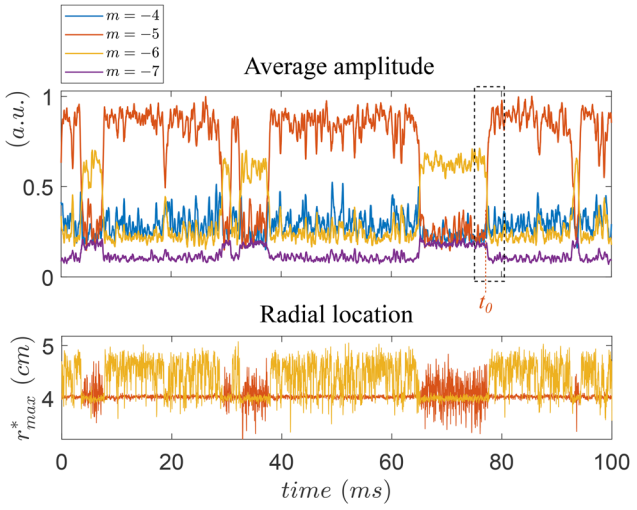

FIG. 5. Time evolution of m-mode average amplitudes extracted by 2D-FT for $p_0 = 1.3$ mTorr.

© Author(s) 2023

since spatial modes structure are deduced from a time-averaged analysis. Figure 5 is further discussed in Sec. V. Now let us compare the results obtained from both POD and 2D-FT analysis.

C. Comparison between POD and 2D Fourier transform

Figure 6 shows snapshots of the $m=-5$ and -6 2D-FT reconstructed modes, as well as the corresponding modes reconstructed from the POD analysis $I_{1,2}^{\mathrm{POD}}$ and $I_{3,4}^{\mathrm{POD}}$ for the experiment achieved at $p_0 = 1.3$ mTorr. The snapshots are shown every 0.06 ms following $t_0 = 77.27$ ms, marking the beginning of an energy exchange between modes $m=-5$ and -6 [see Fig. 5 (top)]. The time interval 0.06 ms represents slightly more than three wave periods for the $m=-5$ mode, and nearly four wave periods for the $m=-6$ mode. The spatial shape of the 2D-FT modes varies significantly. On the contrary, the shapes of the POD reconstructed modes remain almost unchanged. This is actually expected since each of these signals is merely composed of the linear combination of two spatial fields. Note also that the spatial structures Ψ_i were extracted from the time-averaged data field (see Subsection III A): the reconstructed modes are unable to account for spatially localized variations.

Let us now compare the spatial structures provided by POD and 2D-FT. Figure 7 (top) shows time-average radial profiles of the modes for both decompositions. The profiles are computed by an integration along θ, averaged over the 20 000 images. Figure 7 (bottom) shows the azimuthal profiles taken at a given time and for $r^* = 4$ cm. The comparison between POD modes (1 and 2) and the $m=-5$ 2D-FT mode shows an almost perfect match (note that the match slightly decreases

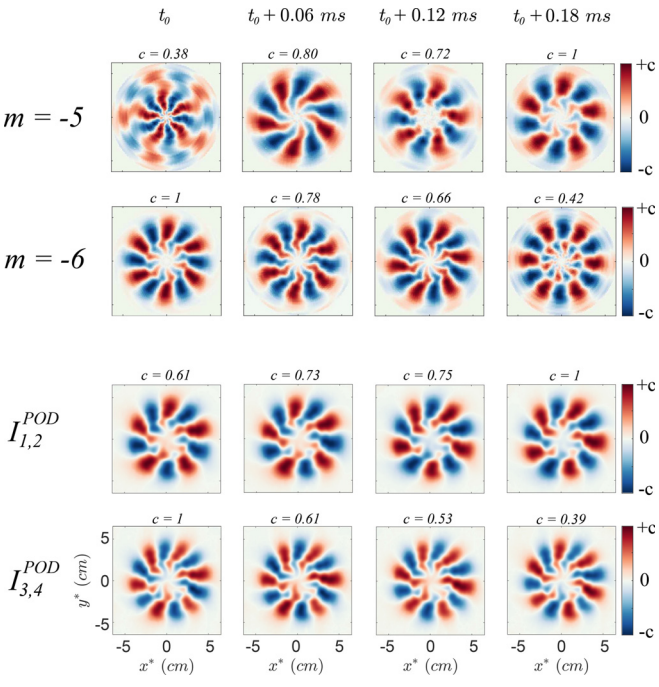

FIG. 6. Evolution of 2D-FT modes $m=-5$ and -6 and POD reconstructed modes $I_{1,2}^{POD}$ and $I_{3,4}^{POD}$ during the exchange event highlighted by the dashed black box in Fig. 5 for $p_0 = 1.3$ mTorr.

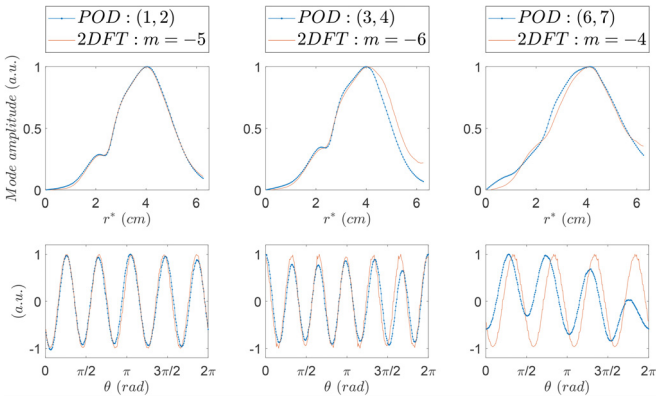

FIG. 7. Comparison of (top) radial and (bottom) azimuthal profiles of the POD and 2D-FT modes at $p_0 = 1.3$ mTorr for the (left) $m=-5$, (center) $m=-6$, and (right) $m=-4$ modes.

when the amplitude of the $m=-5$ mode strongly decreases). The comparison between POD modes (3 and 4) and the $m=-6$ 2D-FT mode gives similar results, although with a lower agreement on the outward part ($r^* \geq 4$ cm) of the radial profiles. An overall good match is observed between the lower amplitude POD modes (6 and 7) and the $m=-4$ 2D-FT mode radial profiles. The instantaneous azimuthal profile are not identical, with a phase shift up to $\sim\pi/8$ depending on the frame. These results show that, in the context of data having 2-π periodicity, POD and 2D-FT decompositions share several common features, while they do provide exactly the same knowledge. Note finally that for the computations performed here with a number of images $N=20\,000$, the POD is twice faster than the 2D-FT (even though it was taken into account for the 2D-FT only 20 mode reconstructions, and half of the images pixels as mentioned in Subsection III B). Then, when only taking $N=2000$, the POD is more than 12 times faster than the 2D-FT.

The main strengths of both POD and 2D-FT techniques are summarized as follows:

- POD is fast and easy. It is extremely simple to implement, and it provides quick and direct results on the spatiotemporal dynamics of a dataset.
- POD is flexible. It does not rely on any particular shape of the physical structure at play, nor on a specific location in the images analyzed. It will, therefore, be particularly well suited to study, for instance, nonlinearly saturated modes exhibiting a complex spatial or temporal pattern. Note, however, that if the results can be particularly insightful, they might also be difficult to interpret (and in some cases, even unusable).
- 2D-FT is explicit, hence robust. Projecting the data onto a predefined set of wave modes (here, for instance, of the form $e^{-i\omega t - im\theta}$) prevents the emergence of unexpected structures, but it provides the results with a well identified physical meaning.
- 2D-FT is exhaustive for linear mode analysis. Since it provides the full spatiotemporal evolution of linear waves, 2D-FT is particularly attractive to study their dynamics, exhibits the corresponding dispersion relations, or uses, for instance, the phase correlations between modes to study weakly nonlinear interactions (see the use of bicoherence in Sec. V).

© Author(s) 2023

Both techniques can provide insightful and complementary results. A recent preprint, reporting on the specific comparison between POD and 2D-FT applied to Hall thruster camera imaging,[52] concludes similarly. Applied to the present datasets, POD shows that the dominant physical structures are m-modes of the form $e^{-i\omega t-im\theta}$. This indicates that the 2D-FT, as implemented here, is an appropriate numerical tool for the mode decomposition. Hence, POD does not constitute a strong gain for further analysis here. In the following, for the identification of the waves and the in-depth study of their weakly nonlinear interactions, we will use the results from the 2D-FT decomposition.

IV. WAVE IDENTIFICATION

The azimuthal waves detected by both POD and 2D-FT are now unambiguously identified as ion acoustic waves. A series of high-speed imaging acquisitions was performed for pressures p_0 in the range [0.8; 2] mTorr by steps of 0.1 mTorr. For each value of the pressure, the radius $r^*_{\max}$ at which the wave amplitude is maximal is deduced from the time-average of the raw images. The experimental phase velocity v_ϕ is determined by a linear fit of the most energetic modes observed on the spectrum $S_{r^*_{\max}}(f,m)$ as $f(m) = v_\phi m/(2\pi r^*_{\max})$. A typical linear fit is shown in Fig. 4 for $p_0 = 1.3$ mTorr. The experimental phase velocities $v_\phi^{\exp}$ are displayed in Fig. 8 as red dots. The error bars are estimated by the combination of the uncertainties on the fit on $S(m, f)$, and on the evaluation of $r^*_{\max}$ [$r^*_{\max}(t)$ fluctuates around its mean value with a standard deviation of ∼3%, see Fig. 5 (bottom)].

These experimental phase velocities are compared to the theoretical ion acoustic speed $c_s = \sqrt{eT_e/m_i}$, with e as the elementary charge and m_i as the ion mass. The computation of the latter requires careful estimates of T_e where the phase velocity is measured on the high-speed images. Note that at $z = 49$ cm, where the probe measurement is performed, the radial position that is best representative of what is seen at $r^* = 3.3$ cm on the images is in fact at $r = 5$ cm (see Appendix A and, for a detailed explanation, see Ref. 27). A detailed pressure scan of the electron temperature T_e was performed with the five-tips probe at a radius $r = 4$ cm, and from a finely resolved radial scan at $p_0 = 1$ mTorr,[27,31] we have $T_e(5\,\text{cm}) \approx T_e(4\,\text{cm}) + 0.2$ eV. Therefore, from the measured values $T_e(4\,\text{cm})$, $T_e(5\,\text{cm})$ is evaluated to lie in the range $[T_e(4\,\text{cm}); T_e(4\,\text{cm}) + 0.5]$ eV. The resulting theoretical ion acoustic speeds $c_s(p_0)$ are shown in Fig. 8 (gray area).

The experimental phase velocities follow the trend of $c_s(p_0)$, with values shifted down by approximately 700 m/s. This is well explained by a Doppler shift due to the plasma column rotation. The plasma column indeed rotates, as was reported previously,[53] where the electric drift $\frac{\vec{E}\times\vec{B}}{B^2} = -\nabla_r\phi_p/B\,\vec{e}_\theta$ was shown to overcome the diamagnetic drift $-\frac{T_i}{n}\frac{\vec{\nabla}n\times\vec{B}}{B^2}$. Two damping mechanisms also need to be accounted for: ion-neutral friction and effective friction due to ionization. The ion-neutral collision frequency reads $\nu_{in} = n_n\sigma_{in}v_{th,i}$, with $v_{th,i} = \sqrt{eT_i(eV)/m_i}$, n_n being the neutral density, and T_i the ion temperature. We consider $n_n \approx p_0/k_BT_n$ with $T_n(p_0) = 350$ K, $\sigma_{\text{in}} = 1.6\times10^{18}$ m^{-2} from experimental cross sections,[54] and $T_i \approx 0.2$ eV using previous LIF measurements. The effective friction due to the ionization originates from ions created with a temperature much lower than the surrounding T_i and depends on the ionization frequency ν_{iz}, computed as $\nu_{iz} = n_nK_{iz,0}T_e^{0.59}\exp(-\varepsilon_{iz}/T_e)$, with $K_{iz,0} = 2.34\times10^{-14}$ m^3/s and $\varepsilon_{iz} = 17.44$ eV, and T_e in eV.[55] A global damping factor K is then given[31,53] as $K = 1 + (\frac{\nu_{in}+\nu_{iz}}{\omega_{ci}})^2$, with ω_{ci} as the ion cyclotron frequency. This finally gives a background azimuthal rotation of the ions as $v_{i0,\theta} \approx -(1/K)\partial_r\phi(r)/B$.

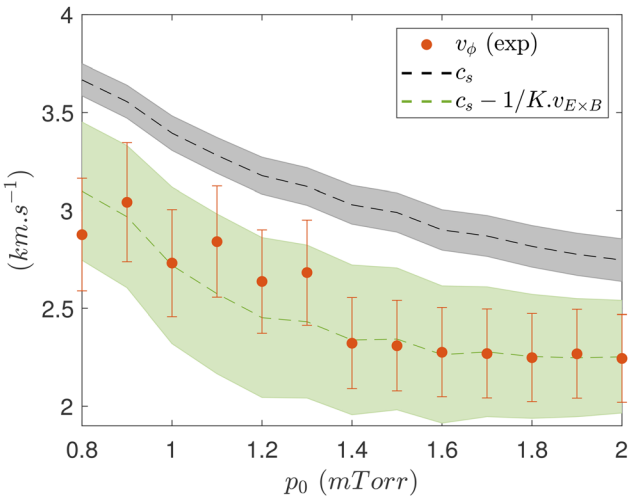

FIG. 8. Comparison between the experimental phase velocity (red dots), the ion sound velocity c_s (black curve), and its Doppler shifted values (green curve).

The rotation velocity $v_{i0,\theta}$ is estimated from the experimental profiles $\phi_p(r)$ shown in Fig. 2 (measured at $p_0 = 1$ mTorr, and assuming variations with pressure within ±20%). The estimated values of n_n and T_i are considered to be bounded within ±10%, and T_e is estimated from $T_e^{r=4cm}(p_0)$ as explained above. The results for the estimate of $c_s + v_{i0,\theta}$ are shown in Fig. 8 (green curve). In spite of all the approximations made, the comparison between experimental phase velocities and the Doppler shifted values of c_s provides a very satisfactory agreement. This allows us to identify with great confidence the azimuthal waves observed at $B = 170$ G as ion acoustic waves. An interesting feature is that the ion acoustic waves travel in the positive θ direction, i.e., opposite to the $E\times B$ drive.

We stress here that adding the ion background velocity to the classical ion acoustic wave speed is a crude approximation, deemed sufficient here for the purpose of wave identification. However, a careful calculation would require to compute a complete dispersion relation from the governing equations, which couple in a complex way and prescribe direct analytical computation. Indeed the effect of an ion background velocity on the ion acoustic phase velocity is likely to be coupled with other effects, such as electron magnetization or friction with the neutrals, leading to computations well beyond the scope of this article.

Interestingly, ion acoustic waves are only observed over a narrow range of magnetic field values. For $B = 80$ G, no clear wave emerges from the fluctuations of the plasma density or emitted light intensity; on the other hand, for $B \geq 300$ G, low frequency waves develop.[31]

V. MODE DYNAMICS AND INTERACTIONS

The spatiotemporal dynamics and the nonlinear nature of the energy exchanges between the ion acoustic modes, as clearly shown in Fig. 5, are now described.

© Author(s) 2023

A. Growth rates of ion acoustic modes

The time series shown in Fig. 6 is taken around the exchange event highlighted at t_0 in Fig. 5. At time t_0, the amplitude of the $m=-6$ mode is close to its maximum, while the amplitude of the $m=-5$ mode is close to its minimum. At time t_0+18 ms, the amplitude of the $m=-6$ mode has decreased close to its minimum value, and the $m=-5$ mode dominates. Figure 5 (bottom) shows that the radial position of the dominant mode (either the $m=-5$ or the -6 mode) is indeed very stable. On the contrary, the radial position of the low amplitude mode strongly fluctuates around its equilibrium value (with standard deviations around 0.6 cm for the $m=-5$ mode and $\sim$0.5 cm for the $m=-6$ mode).

The exchange events observed for $p_0=1.3$ mTorr between modes $m=-5$ and -6 (Figs. 3 and 5) are similarly observed at $p_0=1.1$ and $p_0=0.9$ mTorr. The timescales of the exchange events are now determined at these three values of the pressure. This is done by fitting the mode amplitude A_m as exponentially growing: $A_m \propto \exp(t/\tau)$. Figure 9 (left) shows a typical fit around t_0: the green part shows the interval over which the raw signal (blue) is fitted; a low-pass filtered signal is shown for clarity (red). Figure 9 (right) shows the resulting values of τ found for the $m=-5$ mode. The growth-time τ significantly increases with the pressure, its value doubles from $p_0=0.9$ to 1.3 mTorr. This is interpreted as being the result of an increased friction from the neutrals at higher pressure. Note that this observation of a decrease in the ion acoustic wave growth rate with increasing pressure is consistent with theoretical predictions.[9]

B. Residence time distribution

The statistics of the transitions between the $m=-5$ and -6 modes were obtained in a new set of experiments, performed at a lower sampling frequency (20 kfps)[56] over longer times (2 s). This allows to extract the time evolution of the modes' average amplitude, extracted by 2D-FT. The probability distribution function of the residence time of the $m=-4$, -5, and -6 modes are shown in Fig. 10, for a total duration of 4 s (i.e., more than 1000 transitions between modes). The distributions are compatible with an exponential

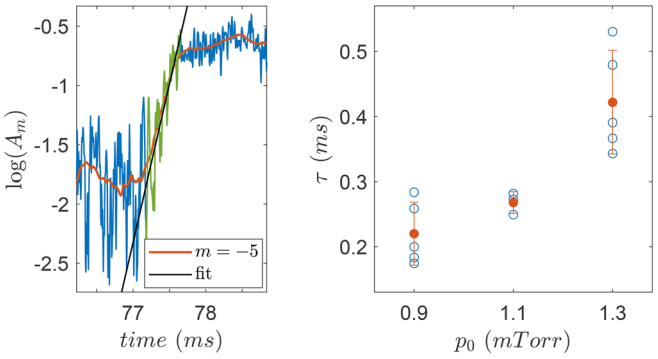

FIG. 9. Left: time evolution of m-mode average amplitudes, extracted by 2D-FT. Left: fit of the 2D-FT $m=-5$ mode growth rate at an exchange event with $m=-6$ mode for $p_0=1.3$ mTorr. The fit is done on a selected interval of the raw data (light blue). The red curve is the result of a filter. Right: evolution of the growth time-scale of $m=-5$ mode, evaluated during exchange events, as a function of the pressure p_0.

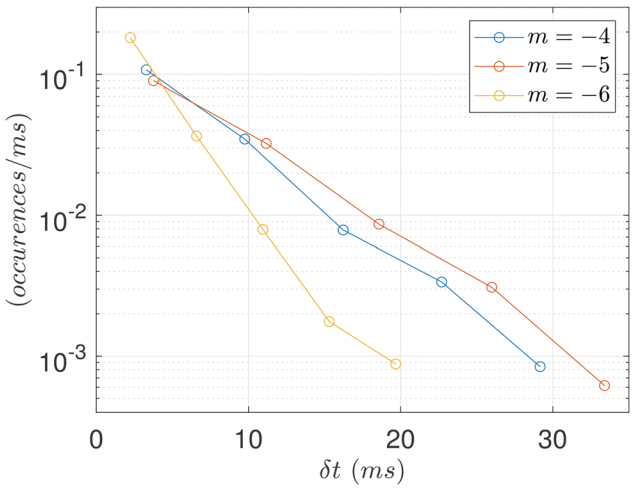

FIG. 10. Residence time PDF, obtained for a neutral pressure $p_0=1.30$ mTorr.

distribution, which implies that the transition events are not correlated. Such distributions of residence times or waiting times are ubiquitous to transitions observed in aerodynamics,[57] turbulent flows,[58,59] or convection;[60] to the waiting time between reversals in dynamo experiments;[61] or the turbulent dynamics of the scrape-off layer in tokamaks.[62,63]

For all modes, the probability distribution function is compatible with a functional fit of the form $e^{-t/\tau}$, with $\tau=5.4$ ms for $m=-4$, and $\tau=6.0$ ms for $m=-5$, and $\tau=3.2$ ms for $m=-6$. As already observed in Fig. 5, the $m=-4$ mode is tied to the $m=-5$ mode, resulting in similar PDF. Figure 5 also shows that the system is more often dominated by a $m=-5$ mode, which results in an exponential PDF with a larger characteristic time for the $m=-5$ mode as compared to the $m=-6$ mode. High-speed imaging of the dynamics of the plasma allows to probe long-time statistics of the wave dynamics. It opens the possibility to probe the evolution of the characteristic residence time as a function of the control parameters (for instance, pressure), possibly shedding light on the physical processes leading to exchange events. Note that the dominant mode (and the associated characteristic time) was observed to strongly evolve with pressure (data not shown and beyond the scope of this article).

C. Nonlinear behavior

In order to further assess the nonlinear nature of the dynamics between the dominant ion acoustic modes, the bicoherence $b^2(f_{m=-5},f_{m=-1})$ is computed for the three-wave interaction $(m=-5)+(m=-1)\leftrightarrow(m=-6)$, and is shown in Fig. 11. Note that to increase statistics, the 2D-FT at all radii $1\le r^*\le 5$ around the wave maximal amplitude is used. More details on the bicoherence computations are provided in Appendix B. The threshold map shown in Fig. 11(a) was computed using a basic surrogate technique where the phases of the 2D-FT signal are randomly mixed. This yields bicoherence values for signals without any preferential phase relations, from which a threshold value of $\max(b_0^2)=0.12$ is estimated. Figure 11(b) shows the map of $b^2(f_{m=-5},f_{m=-1})$ with $f_{m=-5}$ and $f_{m=-1}$, the frequencies of modes $m=-5$ and -1, respectively. For the sake of visibility, the areas of bicoherence high values are highlighted by gray

© Author(s) 2023

contours (defined at 40% of the maximum value of a Gaussian filtered b^2 map). Most of the bicoherence highest values lie around the diagonal $f_{m=-5} + f_{m=-1} = 65$ kHz, that is the dominant frequency of the $m = -6$ mode. This reveals the strong nonlinear behavior of the ($m = -6$ and $f \sim 65$ kHz) mode component, which interacts with $m = -5$ and -1 modes via continuous sets of frequencies. The points displayed as red dots in Fig. 11(b) are also enlarged for clarity: they correspond to $b^2 \gtrsim 0.36$, i.e., more than three times the threshold value. The points for which $f_{m=-1} = 0$, and $f_{m=-5} \in [64.6; 65.4]$ kHz correspond to frequency components of the $m = -5$ mode being fed by the high amplitude of the ($m = -6$ and $f \sim 65$ kHz) component. Note that these interactions are not the dominant processes characterizing the energy exchanges detailed in Subsection V A, since they only involve frequency components of the $m = -5$ mode around 65 kHz with a low energy. The point at $f_{m=-5} = 55.4$ and $f_{m=-1} = 11.2$ kHz, however, corresponds to the interaction,

$$(m = -5, f = 55.4) + (m = -1, f = 11.2) \leftrightarrow (m = -6, f = 66.7),$$

which involves the dominant frequency components of the $m = -5$ and -6 modes. The very high bicoherence value at this location ($b^2 = 0.39$) definitively establishes the nonlinearity of the interactions between the ion acoustic modes ($m = -5, f = 55.4$ kHz) and ($m = -6$, $f = 66.7$ kHz) at the origin of the transitions observed in Fig. 5.

Finally, Fig. 11(c) shows the frequency spectra of the $m = -6$, -5, and -1 modes involved in the three-wave interactions described above. These spectra correspond to 1D cuts along the frequency axis of the 2D-FT spectrum shown in Fig. 4. These spectra clearly display the nonlinear feeding of the $m = -5$ mode by the high amplitude $m = -6$ mode around 65 kHz. The nonlinear feeding of modes $m = -1$ and -6 by the high amplitude $m = -5$ mode around 55 kHz is also visible. The component ($m = -6, f = 55$ kHz) is then nonlinearly interacting with ($m = -5, f = 44$ kHz) and ($m = -1, f = 11$ kHz), as can be deduced by the high values of $b^2(f_{m=-5} \sim 44, f_{m=-1} \sim 11)$ from Fig. 11(b).

The computation of other bicoherence maps (not shown here) reveals additional nonlinear behaviors. The bicoherence computation of the $(m = -6) + (m = -1) \leftrightarrow (m = -7)$ coupling unambiguously shows that ($m = -6, f = 65.2$ kHz) nonlinearly interacts with ($m = -7, f = 74.0$ kHz) via an ($m = -1, f = 8.8$ kHz) mode component [with $b^2 = 0.36 > 3\max(b_0^2)$]. Similarly, bicoherence computation of the $(m = -4) + (m = -1) \leftrightarrow (m = -5)$ coupling highlights that ($m = -4, f = 44.2$ kHz) and ($m = -5, f = 55.4$ kHz) modes nonlinearly interact via ($m = -1, f = 11.2$ kHz) [with $b^2 = 0.38 > 3\max(b_0^2)$]. As a last example, the bicoherence map for the interaction $(m = -4) + (m = -2) \leftrightarrow (m = -6)$ does not exhibit high values, indicating the absence of nonlinear interaction between the corresponding ion acoustic modes. However, it reveals that the frequency components ($f = 55$ kHz) of ($m = -4$) and ($m = -6$) modes (resulting from the spread of the $m = -5$ mode, visible in Fig. 4) are nonlinearly linked via the ($m = -2, f = 0$ kHz) mode component.

Thanks to the rich spatiotemporal information provided by camera imaging and to the use of bicoherence, the weakly nonlinear interactions are clearly highlighted. In particular, the existence of three-wave interactions between ion acoustic modes $m = -p$, $-p - 1$, and -1, for $p \in [4, 5, 6]$, is demonstrated.

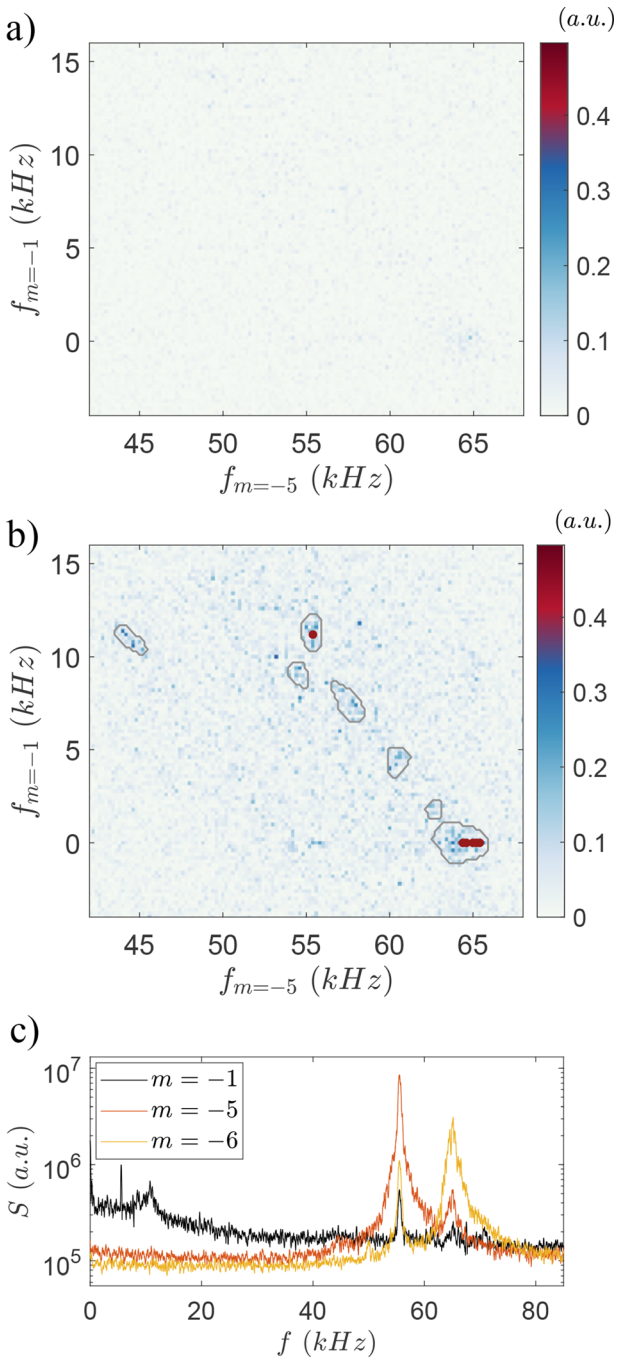

FIG. 11. Maps of the threshold b_0^2 (a) and bicoherence b^2 (b) corresponding to the three-wave interaction $(m = -5) + (m = -1) \leftrightarrow (m = -6)$. (c) Frequency power spectra of modes $m = -1$, -5, and -6 from 2D-FT computed at $r^* = 3.3$ cm. $B = 170$ G and $p_0 = 1.3$ mTorr.

VI. CONCLUSION

We have presented the first report of temporally and spatially entirely resolved ion acoustic waves in a magnetized plasma column.

© Author(s) 2023

The ion acoustic waves were observed by means of fast camera imaging in a low temperature argon plasma column, with dominant azimuthal mode numbers $m = -4$, -5, and -6, depending on the neutral pressure that was varied from 0.8 to 2 mTorr.

Two image analysis techniques, namely, proper orthogonal decomposition (POD) and 2D Fourier transform (2D-FT), were presented and thoroughly compared. These tools are found to be complementary. POD is easy to implement and adaptable to any type of data, and it is useful to provide a fast overview of the underlying dynamics of a given dataset. This helps focusing in a second time on a more precise and targeted analysis, that 2D-FT can then provide, yielding detailed and unambiguous information.

Using 2D-FT analysis of high-speed images, the ion acoustic waves were found to rotate in an opposite direction to the global $E \times B$ drift of the plasma column, with a phase velocity Doppler shifted by this actual electric drift velocity.

The dynamics of the dominant ion acoustic modes was then explored using the 2D-FT decomposition. Growth rates, which extraction was made possible by the camera high temporal resolution, were found to decrease as pressure increases, following previous numerical predictions. A detailed analysis was then carried out in the particular case of $p_0 = 1.3$ mTorr. At this pressure, the exchange dynamics between dominant modes $m = -5$ and -6 was shown to be of a bistable nature. More generally, the weakly nonlinear nature of the $m = -p$ and $-p-1$ mode interaction ($p \in [4, 5, 6]$), involved in a three-wave interaction with a $m = -1$ mode, was demonstrated by means of bicoherence computation.

Finally, we emphasize that, except from probe measurements that were needed for the wave identification, all the results that were presented exclusively rely on fast camera imaging measurements. This work can, therefore, be considered as a case study demonstrating the very powerful capabilities of fast camera imaging as a plasma diagnostics, notably for the exploration of complex waves dynamics.

ACKNOWLEDGMENTS

This work was partly supported by the French National Research Agency under Contract No. ANR-13-JS04-0003-01. We acknowledge support from the CNRS for the acquisition of the high-speed camera, useful discussions with V. Désangles and G. Bousselin, and warmly thank P. Borgnat for advice on surrogate techniques.

AUTHOR DECLARATIONS

Conflict of Interest

The authors have no conflicts to disclose.

Author Contributions

Simon Vincent: Conceptualization (lead); Data curation (lead); Formal analysis (lead); Investigation (lead); Resources (equal); Software (equal); Writing – original draft (lead); Writing – review & editing (lead). **Vincent Dolique:** Conceptualization (supporting); Data curation (supporting); Formal analysis (supporting); Investigation (supporting); Resources (equal); Software (equal); Writing – original draft (supporting); Writing – review & editing (supporting). **Nicolas Plihon:** Conceptualization (supporting); Data curation (supporting); Formal analysis (supporting); Funding acquisition (lead); Investigation (supporting); Resources (equal); Software (equal); Writing – original draft (supporting); Writing – review & editing (supporting).

DATA AVAILABILITY

The data that support the findings of this study are available from the corresponding author upon reasonable request.

APPENDIX A: RADIAL SCALE: CAMERA IMAGING VS PROBE

The magnetic field ripple and parallax in our experimental setup leads the camera lines of sight to cross regions of different plasma parameters. The light recorded by camera, resulting from an integration process along these lines of sight, cannot be directly compared to probe measurements that are performed at $z = L_2$.

A transformation is implemented, modeling the integration along the camera lines of sight of any plasma parameter that is measured at $z = L_2$. The details of this transformation are provided in Ref. 27.

Figure 12 shows the result of this artificial integration process, applied to a test profile, peaked at $r = 5$ cm (blue curve). The resulting profile (red curve), expressed along the camera imaging coordinate r^*, shows that what is seen on the camera images at $r^* = 3.3$ cm mainly corresponds to the plasma parameter evolution that is located at $r = 5$ cm on the axis $z = L_2$.

APPENDIX B: BICOHERENCE AND CONFIDENCE LEVEL

Bicoherence is a spectral analysis tool that is commonly used in physics for the detection of nonlinear three-wave interactions. Bicoherence computation essentially consists in extracting the frequency components of one of several signals and comparing their phases. The signal decomposition at the basis of a bicoherence analysis can be done by Fourier transform[64,65] as it is the case in this work, or based on a wavelet approach.[66,67] In this Appendix, we first remind the basic principle of bicoherence, and then explain how bicoherence is computed in the particular case of camera images. Then, we provide the definition of a clear and mathematically meaningful threshold, which is often lacking when bicoherence is used onto experimental data in plasma physics.

1. Evaluation of three-wave interactions by bicoherence

Let us consider three signals x, y, and z with corresponding Fourier transforms $\hat{x}$, $\hat{y}$, and $\hat{z}$. The cross bispectrum of x, y, and z is defined as a function of frequencies (f_1, f_2) as

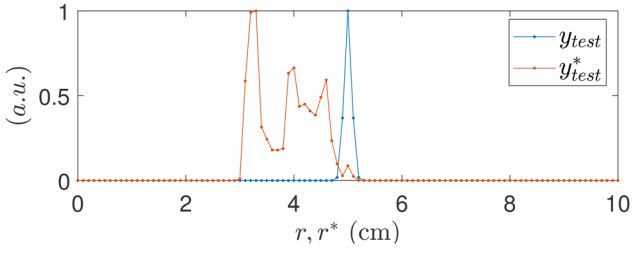

FIG. 12. Camera lines of sight integration process applied to a test profile measured at $z = L_2$.

© Author(s) 2023

$B(f_1,f_2) = \hat{x}(f_1)\hat{y}(f_2)\hat{z}^*(f_1+f_2)$. If the frequency components f_1 and f_2 of x and y, respectively, (with phases ϕ_1^x and ϕ_2^y) are involved in a three-wave interaction with the frequency component f_1+f_2 of z (with a phase ϕ_{1+2}^z), the phase difference between these signals is a constant. Computing the bispectrum onto successive reduced parts δ_t of the signals is, therefore, a way of measuring this phase locking, since $B_{\delta t}(f_1,f_2) \propto \exp^{-i(\phi_1^x+\phi_2^y-\phi_{1+2}^z)}$. The bicoherence is defined by the normalized average over a statistically significant number of such bispectrum computations as follows:

$$b^2(f_1,f_2) = \frac{|\langle \hat{x}(f_1)\cdot\hat{y}(f_2)\cdot\hat{z}^*(f_1+f_2)\rangle_{\delta_t}|^2}{\langle|\hat{x}(f_1)\cdot\hat{y}(f_2)|^2\rangle_{\delta_t}\langle|\hat{z}(f_1+f_2)|^2\rangle_{\delta_t}}.$$

If the signal frequency components previously mentioned are perfectly uncorrelated, b^2 corresponds to the average of random complex numbers, and tends to cancel out. If those frequency components are on the contrary perfectly phase locked, the computations of $B_{\delta t}(f_1,f_2)$ have a constant value and $b^2=1$. In the case of experimental data, neither case is realistic, and a threshold value b_0^2 above which the bicoherence can be considered significant needs to be defined (see the last paragraph of this Appendix).

2. Bicoherence on camera images

With camera images that provide 2D spatiotemporal signals, bicoherence can be computed between the frequency components of distinct modes m. Bicoherence allows to probe the phases of signal components for a given set of wave vector and frequency (m,f). This analysis is applied on the present camera images, following the work of Ref. 46. For a given radius r^*, let us denote the 2D Fourier decomposition of the light intensity as follows:

$$A(t,\theta) = \sum_{n,p} a(f_n,m_p)e^{i(2\pi f_n t - m_p\theta + \phi_{n,p})}.$$

The spectrum associated with a single m_p mode is a part of this decomposition,

$$\hat{A}_{m_p}(f_n) = a(f_n,m_p)e^{i\phi_{n,p}}.$$

Similar to the computations achieved for 1D signals, the bispectrum is defined as a statistical averaging, over parts of lengths δt of the signal. In order to improve the statistical averaging here, the sum is also done over the signals from various radii r^*. This double averaging process is denoted $\langle\cdot\rangle_{r^*,\delta_t}$. The bispectrum between components (m_1,f_1) and (m_2,f_2) is then defined as $B_{m_1,m_2}(f_1,f_2) = \hat{A}_{m_1}(f_1)\cdot\hat{A}_{m_2}(f_2)\cdot\hat{A}_{m_1+m_2}(f_1+f_2)^*$, and the bicoherence is computed as

$$b^2_{m_1,m_2}(f_1,f_2) = \frac{|\langle \hat{A}_{m_1}(f_1)\cdot\hat{A}_{m_2}(f_2)\cdot\hat{A}^*_{m_1+m_2}(f_1+f_2)\rangle_{r^*,\delta_t}|^2}{\langle|\hat{A}_{m_1}(f_1)\cdot\hat{A}_{m_2}(f_2)|^2\rangle_{r^*,\delta_t}\langle|\hat{A}_{m_1+m_2}(f_1+f_2)|^2\rangle_{r^*,\delta_t}}.$$

The bicoherence as it is implemented in our code takes mode numbers m_1 and m_2 as an entry and explores all possible three-wave interactions $(m_1,f_1)+(m_2,f_2)\leftrightarrow(m_1+m_2,f_1+f_2)$ in terms of frequencies f_1 and f_2. The operation is fixed as an addition, and the result is in a form of a 2D map of $b^2_{m_1,m_2}(f_1,f_2)$, with $[f_1,f_2]\in[0,F_s/2]^2$, F_s being the data sampling frequency. Here, for simplicity, the bicoherence applied to camera images is simply denoted b^2.

3. Definition of a threshold

The phase correlation between any set of experimental signals is likely to be imperfect or partial, leading to $0<b^2<1$. Moreover, the absolute values of the bicoherence are relative to each set of signals investigated: a general threshold value is not relevant. A method to systematically determine the level above which the value of b^2 becomes physically meaningful, which depends on each bicoherence computation, is therefore needed.

A possible method consists in the creation of an artificial set of signals, sharing the same characteristics than the original signals, but without any preferential relation between its frequency components. The bicoherence of this artificial set of signals is then computed, providing a lower limit for the values of b^2. This type of method is called a surrogate technique,[68] and it can be very sophisticated. Here, we use a very basic version of the surrogate technique: the phases of each 2D-FT spectra are randomly mixed. The bicoherence computation applied to this modified data defines a threshold map $b_0^2(f_1,f_2)$. Then for simplicity, we take the maximal value $\max(b_0^2)$ and define it as a global threshold value for the real bicoherence computation $b^2(f_1,f_2)$ of this dataset.

REFERENCES

[1]D. A. Gurnett and L. A. Frank, "Ion acoustic waves in the solar wind," J. Geophys. Res. **83**, 58–74, https://doi.org/10.1029/JA083iA01p00058 (1978).
[2]D. A. Gurnett, E. Marsch, W. Pilipp, R. Schwenn, and H. Rosenbauer, "Ion acoustic waves and related plasma observations in the solar wind," J. Geophys. Res. **84**, 2029–2038, https://doi.org/10.1029/JA084iA05p02029 (1979).
[3]F. S. Mozer, I. Y. Vasko, and J. L. Verniero, "Triggered ion-acoustic waves in the solar wind," Astrophys. J. Lett. **919**, L2 (2021).
[4]J.-E. Wahlund, P. Louarn, T. Chust, H. de Feraudy, and A. Roux, "On ion acoustic turbulence and the nonlinear evolution of kinetic Alfvén waves in aurora," Geophys. Res. Lett. **21**, 1831–1834, https://doi.org/10.1029/94GL01289 (1994).
[5]H. Ikezi, "Experiments on ion-acoustic solitary waves," Phys. Fluids **16**(10), 1668–1675 (1973).
[6]T. Sato and H. Okuda, "Ion-acoustic double layers," Phys. Rev. Lett. **44**, 740–743 (1980).
[7]N. Plihon and P. Chabert, "Ion acoustic waves and double-layers in electronegative expanding plasmas," Phys. Plasmas **18**(8), 082102 (2011).
[8]N. D'Angelo, S. V. Goeler, and T. Ohe, "Propagation and damping of ion waves in a plasma with negative ions," Phys. Fluids **9**(8), 1605–1606 (1966).
[9]S. D. Baalrud, "Influence of ion streaming instabilities on transport near plasma boundaries," Plasma Sources Sci. Technol. **25**, 025008 (2016).
[10]L. P. Beving, M. M. Hopkins, and S. D. Baalrud, "Simulations of ion heating due to ion-acoustic instabilities in presheaths," Phys. Plasmas **28**, 123516 (2021).
[11]D. Lee, G. Severn, L. Oksuz, and N. Hershkowitz, "Laser-induced fluorescence measurements of argon ion velocities near the sheath boundary of an argon–xenon plasma," J. Phys. D **39**, 5230–5235 (2006).
[12]L. Oksuz, D. Lee, and N. Hershkowitz, "Ion acoustic wave studies near the presheath/sheath boundary in a weakly collisional argon/xenon plasma," Plasma Sources Sci. Technol. **17**, 015012 (2008).
[13]A. M. Hala and N. Hershkowitz, "Ion acoustic wave velocity measurement of the concentration of two ion species in a multi-dipole plasma," Rev. Sci. Instrum. **72**, 2279 (2001).
[14]B. A. Jorns, C. Dodson, D. M. Goebel, and R. Wirz, "Propagation of ion acoustic wave energy in the plume of a high-current lab6 hollow cathode," Phys. Rev. E **96**, 023208 (2017).
[15]S. Tsikata, K. Hara, and S. Mazouffre, "Characterization of hollow cathode plasma turbulence using coherent Thomson scattering," J. Appl. Phys. **130**, 243304 (2021).

© Author(s) 2023

[16]I. Katz, A. L. Ortega, B. Jorns, and I. G. Mikellides, "Growth and saturation of ion acoustic waves in Hall thrusters," AIAA Paper No. AIAA 2016-4534, 2016.
[17]S. J. Doyle, A. Bennet, D. Tsifakis, J. P. Dedrick, R. W. Boswell, and C. Charles, "Characterization and control of an ion-acoustic plasma instability downstream of a diverging magnetic nozzle," Front. Phys. **8**, 24 (2020).
[18]R. W. Boswell and M. J. Giles, "Trapping of decay waves in whistler resonance cones," Phys. Rev. Lett. **36**, 1142 (1976).
[19]V. F. Virko, G. S. Kirichenko, and K. P. Shamrai, "Parametric ion-acoustic turbulence in a helicon discharge," Plasma Sources Sci. Technol. **12**, 217–224 (2003).
[20]C. S. Corr, N. Plihon, P. Chabert, O. Sutherland, and R. W. Boswell, "Spatially limited ion acoustic wave activity in low-pressure helicon discharges," Phys. Plasmas **11**, 4596 (2004).
[21]A. S. Belov and G. A. Markov, "Generation of ion-acoustic and magnetoacoustic waves in an RF helicon discharge," Plasma Phys. Rep. **32**, 759–764 (2006).
[22]B. Lorenz, M. Krämer, V. L. Selenin, and Y. M. Aliev, "Excitation of short-scale fluctuations by parametric decay of helicon waves into ion–sound and trivelpiece–Gould waves," Plasma Sources Sci. Technol. **14**, 623–635 (2005).
[23]M. Krämer, Y. M. Aliev, A. B. Altukhov, A. D. Gurchenko, E. Z. Gusakov, and K. Niemi, "Anomalous helicon wave absorption and parametric excitation of electrostatic fluctuations in a helicon-produced plasma," Plasma Phys. Controlled Fusion **49**, A167–A175 (2007).
[24]C. S. Corr and R. W. Boswell, "Nonlinear instability dynamics in a high-density, high-beta plasma," Phys. Plasmas **16**, 022308 (2009).
[25]N. Plihon, G. Bousselin, F. Palermo, J. Morales, W. J. T. Bos, F. Godeferd, M. Bourgoin, J.-F. Pinton, M. Moulin, and A. Aanesland, "Flow dynamics and magnetic induction in the von-Kármán plasma experiment," J. Plasma Phys. **81**, 345810102 (2015).
[26]H. Y. W. Tsui, R. D. Bengtson, G. X. Li, H. Lin, M. Meier, C. P. Ritz, and A. J. Wootton, "A new scheme for Langmuir probe measurement of transport and electron temperature fluctuations," Rev. Sci. Instrum. **63**, 4608 (1992).
[27]S. Vincent, V. Dolique, and N. Plihon, "High-speed imaging of magnetized plasmas: When electron temperature matters," Phys. Plasmas **29**, 032104 (2022).
[28]S. Oldenbürger, C. Brandt, F. Brochard, N. Lemoine, and G. Bonhomme, "Spectroscopic interpretation and velocimetry analysis of fluctuations in a cylindrical plasma recorded by a fast camera," Rev. Sci. Instrum. **81**, 063505 (2010).
[29]A. D. Light, S. C. Thakur, Y. Sechrest, C. Brandt, G. R. Tynan, and T. Munsat, "Direct extraction of coherent mode properties from imaging measurements in a linear plasma column," Phys. Plasmas **20**, 082120 (2013).
[30]S. C. Thakur, C. Brandt, A. D. Light, L. Cui, J. J. Gosselin, and G. R. Tynan, "Simultaneous use of camera and probe diagnostics to unambiguously identify and study the dynamics of multiple underlying instabilities during the route to plasma turbulence," Rev. Sci. Instrum **85**, 11E813 (2014).
[31]S. Vincent, "Azimuthal waves modification by current injection in a magnetized plasma column," Ph.D. thesis (Université de Lyon, 2021).
[32]S. C. Thakur, C. Brandt, L. Cui, J. J. Gosselin, A. D. Light, and G. R. Tynan, "Multi-instability plasma dynamics during the route to fully developed turbulence in a helicon plasma," Plasma Sources Sci. Technol. **23**, 044006 (2014).
[33]G. Berkooz, P. Holmes, and J. L. Lumley, "The proper orthogonal decomposition in the analysis of turbulent flows," Annu. Rev. Fluid Mech. **25**, 539–575 (1993).
[34]J. L. Lumley, "The structure of inhomogeneous turbulent flows," *Atmospheric Turbulence and Radio Wave Propagation* (Nauka, 1967), pp. 166–178.
[35]S. Benkadda, T. Dudok de Wit, A. Verga, A. Sen, X. Garbet, and ASDEX Team, "Characterization of coherent structures in tokamak edge turbulence," Phys. Rev. Lett. **73**, 3403 (1994).
[36]B. P. van Milligen, E. Sánchez, A. Alonso, M. A. Pedrosa, C. Hidalgo, A. Martín de Aguilera, and A. L. Fraguas, "The use of the biorthogonal decomposition for the identification of zonal flows at TJ-II," Plasma Phys. Controlled Fusion **57**, 025005 (2015).
[37]C. Hansen, B. Victor, K. Morgan, T. Jarboe, A. Hossack, G. Marklin, B. A. Nelson, and D. Sutherland, "Numerical studies and metric development for validation of magnetohydrodynamic models on the HIT-SI experiment," Phys. Plasmas **22**, 056105 (2015).
[38]T. Dudok de Wit, A. L. Pecquet, J. C. Vallet, and R. Lima, "The biorthogonal decomposition as a tool for investigating fluctuations in plasmas," Phys. Plasmas **1**, 3288 (1994).
[39]H. Tanaka, N. Ohno, Y. Tsuji, and S. Kajita, "2D statistical analysis of non-diffusive transport under attached and detached plasma conditions of the linear divertor simulator," Contrib. Plasma Phys. **50**, 256–266 (2010).
[40]S. M. Angelini, J. P. Levesque, M. E. Mauel, and G. A. Navratil, "High-speed imaging of the plasma response to resonant magnetic perturbations in HBT-EP," Plasma Phys. Controlled Fusion **57**, 045008 (2015).
[41]V. Désangles, S. Shcherbanev, T. Charoy, N. Clément, C. Deltel, P. Richard, S. Vincent, P. Chabert, and A. Bourdon, "Fast camera analysis of plasma instabilities in Hall effect thrusters using a POD method under different operating regimes," Atmosphere **11**, 518 (2020).
[42]G. Becatti, D. M. Goebel, and M. Zuin, "Observation of rotating magnetohydrodynamic modes in the plume of a high-current hollow cathode," J. Appl. Phys. **129**, 033304 (2021).
[43]N. Aubry, "On the hidden beauty of the proper orthogonal decomposition," Theor. Comput. Fluid Dyn. **2**, 339–352 (1991).
[44]Due to the very high frequency of the waves (75 kHz) relative to the sampling frequency (200 kHz), the signals a_1 and a_2 are closer to triangular than sinusoidal shapes; but other measurements of lower frequency waves clearly show sinusoidal evolutions for the a_i signals.
[45]A. Latten, T. Klinger, A. Piel, and T. Pierre, "A probe array for the investigation of spatio-temporal structures in drift wave turbulence," Rev. Sci. Instrum. **66**, 3254 (1995).
[46]T. Yamada, S.-I. Itoh, S. Inagaki, Y. Nagashima, S. Shinohara, N. Kasuya, K. Terasaka, K. Kamatakia, H. Arakawa, M. Yagi, A. Fujisawa, and K. Itoh, "Two-dimensional bispectral analysis of drift wave turbulence in a cylindrical plasma," Phys. Plasmas **17**, 052313 (2010).
[47]C. Brandt, O. Grulke, T. Klinger, J. Negrete, Jr., G. Bousselin, F. Brochard, G. Bonhomme, and S. Oldenbürger, "Spatiotemporal mode structure of nonlinearly coupled drift wave modes," Phys. Rev. E **84**, 056405 (2011).
[48]C. Brandt, S. C. Thakur, A. D. Light, J. Negrete, Jr., and G. R. Tynan, "Spatiotemporal splitting of global eigenmodes due to cross-field coupling via vortex dynamics in drift wave turbulence," Phys. Rev. Lett. **113**, 265001 (2014).
[49]S. Ohdachi, S. Inagaki, T. Kobayashi, and M. Goto, "2D turbulence structure observed by a fast framing camera system in linear magnetized device PANTA," J. Phys.: Conf. Ser. **823**, 012009 (2017).
[50]S. Mazouffre, L. Grimaud, S. Tsikata, K. Matyash, and R. Schneider, "Rotating spoke instabilities in a wall-less Hall thruster: Experiments," Plasma Sources Sci. Technol. **28**(5), 054002 (2019).
[51]I. Romadanov, Y. Raitses, and A. Smolyakov, "Control of coherent structures via external drive of the breathing mode," Plasma Phys. Rep. **45**(2), 134–146 (2019).
[52]J. W. Brooks, M. S. McDonald, and A. A. Kaptanoglu, "A comparison of Fourier and pod mode decomposition methods for high-speed hall thruster video," arXiv:2205.14207v1 (2022).
[53]V. Désangles, G. Bousselin, A. Poye, and N. Plihon, "Rotation and shear control of a weakly magnetized plasma column using current injection by emissive electrodes," J. Plasma Phys. **87**, 905870308 (2021).
[54]A. V. Phelps, "The application of scattering cross sections to ion flux models in discharge sheaths," J. Appl. Phys. **76**, 747 (1994).
[55]M. A. Lieberman and A. J. Lichtenberg, *Principles of Plasma Discharges and Materials Processing*, 2nd ed. (John Wiley and Sons, 2005).
[56]Note that with the lower sampling frequency of 20 kfps, the extracted IAW modes with frequencies ∼70 kHz cannot be resolved temporally, which prevents the distinction between modes $+m$ and $-m$ for a given integer m. However, it is observed that in the same conditions, with higher sampling frequency acquisition, the (m = +p) mode amplitude is negligible in front of the (m = −p) amplitude for $p = [4, 7]$. Therefore, we use at $F_s = 20$ kfps, the sum of the amplitudes of extracted modes +p and −p to estimate the amplitude of mode (m = −p) for $p = [4, 7]$.
[57]A. Gayout, M. Bourgoin, and N. Plihon, "Rare event-triggered transitions in aerodynamic bifurcation," Phys. Rev. Lett. **126**, 104501 (2021).
[58]F. Ravelet, L. Marié, A. Chiffaudel, and F. Daviaud, "Multistability and memory effect in a highly turbulent flow: Experimental evidence for a global bifurcation," Phys. Rev. Lett. **93**, 164501 (2004).

© Author(s) 2023

[59]A. de la Torre and J. Burguete, "Slow dynamics in a turbulent von Kármán swirling flow," Phys. Rev. Lett. **99**, 054101 (2007).
[60]E. Brown and G. Ahlers, "Rotations and cessations of the large-scale circulation in turbulent Rayleigh–Bénard convection," J. Fluid Mech. **568**, 351–386 (2006).
[61]R. Monchaux, M. Berhanu, S. Aumaître, A. Chiffaudel, F. Daviaud, B. Dubrulle, F. Ravelet, S. Fauve, N. Mordant, F. Pétrélis, M. Bourgoin, P. Odier, J.-F. Pinton, N. Plihon, and R. Volk, "The von Kármán sodium experiment: Turbulent dynamical dynamos," Phys. Fluids **21**(3), 035108 (2009).
[62]O. E. Garcia, J. Horacek, and R. A. Pitts, "Intermittent fluctuations in the TCV scrape-off layer," Nucl. Fusion **55**(6), 062002 (2015).
[63]A. Theodorsen, O. E. Garcia, R. Kube, B. LaBombard, and J. L. Terry, "Universality of Poisson-driven plasma fluctuations in the Alcator C-Mod scrape-off layer," Phys. Plasmas **25**(12), 122309 (2018).
[64]C. P. Ritz, E. J. Powers, T. L. Rhodes, R. D. Bengtson, K. W. Gentle, H. Lin, P. E. Phillips, and A. J. Wootton, "Advanced plasma fluctuation analysis techniques and their impact on fusion research," Rev. Sci. Instrum. **59**, 1739 (1988).
[65]S.-I. Itoh, K. Itoh, Y. Nagashima, and Y. Kosuga, "On the application of cross bispectrum and cross bicoherence," Plasma Fusion Res. **12**, 1101003 (2017).
[66]B. Ph. van Milligen, E. Sanchez, T. Estrada, C. Hidalgo, B. Brafias, B. Carreras, and L. Garda, "Wavelet bicoherence: A new turbulence analysis tool," Phys. Plasmas **2**, 3017 (1995).
[67]S. Oldenbürger, F. Brochard, and G. Bonhomme, "Investigation of mode coupling in a magnetized plasma column using fast imaging," Phys. Plasmas **18**, 032307 (2011).
[68]K. L. Siu and K. H. Chon, "On the efficacy of the combined use of the cross-bicoherence with surrogate data technique to statistically quantify the presence of nonlinear interactions," Ann. Biomed. Eng. **37**, 1839–1848 (2009).

© Author(s) 2023